Rapid gate-based spin read-out in silicon using an on-chip resonator

Zheng, Guoji; Samkharadze, Nodar; Noordam, Marc L.; Kalhor, Nima; Brousse, Delphine; Sammak, Amir; Scappucci, Giordano; Vandersypen, Lieven M.K.

DOI
10.1038/s41565-019-0488-9

Publication date
2019

Document Version
Final published version

Published in
Nature Nanotechnology

LETTERS
https://doi.org/10.1038/s41565-019-0488-9

nature nanotechnology

Corrected: Author Correction

Rapid gate-based spin read-out in silicon using an on-chip resonator

Guoji Zheng[1], Nodar Samkharadze[1,2], Marc L. Noordam[1], Nima Kalhor[1], Delphine Brousse[2], Amir Sammak[2], Giordano Scappucci[1] and Lieven M. K. Vandersypen[1*]

Silicon spin qubits are one of the leading platforms for quantum computation[1,2]. As with any qubit implementation, a crucial requirement is the ability to measure individual quantum states rapidly and with high fidelity. Since the signal from a single electron spin is minute, the different spin states are converted to different charge states[3,4]. Charge detection, so far, has mostly relied on external electrometers[5–7], which hinders scaling to two-dimensional spin qubit arrays[2,8,9]. Alternatively, gate-based dispersive read-out based on off-chip lumped element resonators has been demonstrated[10–13], but integration times of 0.2–2 ms were required to achieve single-shot read-out[14–16]. Here, we connect an on-chip superconducting resonant circuit to two of the gates that confine electrons in a double quantum dot. Measurement of the power transmitted through a feedline coupled to the resonator probes the charge susceptibility, distinguishing whether or not an electron can oscillate between the dots in response to the probe power. With this approach, we achieve a signal-to-noise ratio of about six within an integration time of only 1 µs. Using Pauli's exclusion principle for spin-to-charge conversion, we demonstrate single-shot read-out of a two-electron spin state with an average fidelity of >98% in 6 µs. This result may form the basis of frequency-multiplexed read-out in dense spin qubit systems without external electrometers, therefore simplifying the system architecture.

Single-shot read-out is required to implement quantum error correcting schemes, where the measurement and correction should be performed with high fidelity and well within the qubit coherence times (that is, with high bandwidth). In gate-based sensing, a technique using radiofrequency reflectometry[7] is applied to a single gate that is already in place to define the quantum dot[17–19]. However, resonant circuits, so far, have made use of commercial or superconducting inductors mounted on a printed circuit board adjacent to the quantum dot chip. These circuits are quite lossy and contain large parasitic capacitances, masking the useful signal from the capacitive response of the quantum dots. Although single-shot read-out of spin states could be achieved thanks to long spin relaxation timescales, the effective detection bandwidths were limited by the signal-to-noise ratio (SNR) to a few kilohertz[14–16].

Here, we fully integrate an on-chip superconducting microwave resonator into a Si/SiGe double quantum dot (DQD) device[20] to perform single-shot singlet-triplet read-out (Fig. 1a,c). Two gates are galvanically connected to the NbTiN nanowire resonator with a high characteristic impedance of ~1 kΩ[21]. The resonator is probed through a capacitively coupled planar transmission line (feedline) with an average population of three photons (see Methods and Supplementary Fig. 2 for the measurement set-up). The observed dip in the normalized transmission amplitude of the probe signal reveals the resonance frequency $f_0 = 5.7116$ GHz, as well as the total linewidth $\kappa/2\pi \approx 2.2$ MHz (Fig. 1b), which sets the maximum measurement bandwidth. The high quality factor ($Q \approx 2{,}600$) and large impedance of the resonator enable fast high-fidelity charge detection.

The resonator is a sensitive probe that can detect tiny changes in the charge susceptibility of the DQD[22–26]. The susceptibility is largest at zero detuning, $\varepsilon = 0$, where the electrochemical potentials of the left and right dots align and an electron is able to tunnel freely between the two dots. In this case, the DQD damps the resonator and shifts its frequency. Away from zero detuning, the electron(s) can only move within a quantum dot, and the electrical susceptibility is negligible in comparison. By recording the transmitted signal at the resonance frequency f_0 while varying the voltages on the plunger gates, LP and RP, one can map out the charge stability diagram of the DQD. A typical diagram in the few-electron regime is shown in Fig. 2a, where (N_L,N_R) indicates the charge occupation, with N_L (N_R) the number of electrons in the left (right) dot (Supplementary Fig. 1). A bright yellow line appears at the transition between the (1,1) and (0,2) charge states. Because the probe frequency of ~5.7 GHz is above the interdot tunnel coupling $t_c \approx 2$ GHz, measured using two-tone spectroscopy[27] (data not shown), the system is not in the adiabatic limit where quantum capacitance arising from the curvature of the dispersion relation dominates the response[28]. Instead, there is also a significant contribution from the tunnelling capacitance, whereby charges non-adiabatically redistribute in the double dot at a rate comparable to the probe frequency.

We first quantify the sensitivity of the resonator to changes in the DQD susceptibility due to electron tunnelling. We scan over the interdot transition by sweeping the voltage on RP (red dashed line in Fig. 2a). Figure 2b shows two examples of the resulting line traces at P = −110 dBm, with integration times of 1.28 µs (blue) and 256 µs (red) per point. The power SNR is defined as $\mathrm{SNR} = (A/B)^2$. The signal A is the difference between the transmitted amplitude at the interdot transition ($V_{RP} \approx -162$ mV) and the amplitude in the Coulomb blockaded region, where no electrons are allowed to tunnel. This difference is obtained from a Gaussian fit to data such as that in Fig. 2b. The noise B is the r.m.s. noise amplitude measured with the electrons in Coulomb blockade ($V_{RP} \approx -170$ mV). We expect A^2 to increase linearly with probe power, and B^2 to decrease linearly with integration time. Figure 2c shows the SNR as a function of the integration time for three different probe powers.

[1]QuTech and Kavli Institute of Nanoscience, Delft University of Technology, Delft, The Netherlands. [2]QuTech and Netherlands Organization for Applied Scientific Research (TNO), Delft, The Netherlands. *e-mail: l.m.k.vandersypen@tudelft.nl

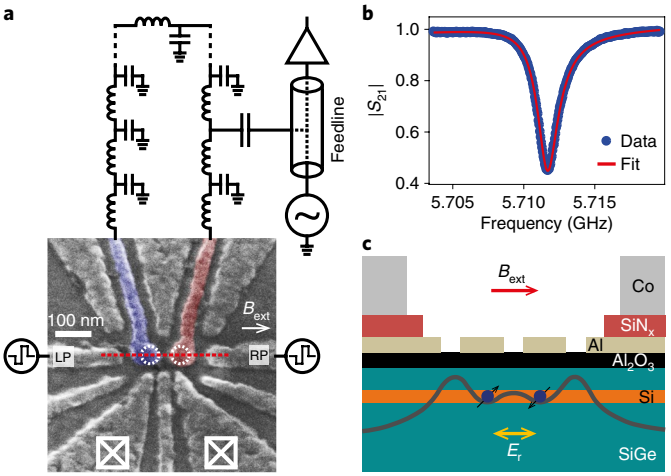

Fig. 1 | Device schematics. a, Scanning electron micrograph of a device nominally identical to that used in the experiment, showing a single layer of Al gate electrodes for accumulation and confinement of electrons, with a schematic of the superconducting resonator. The circuit consists of a NbTiN thin wire with a $\lambda/2$ resonance mode. The ends of the wire—the purple and red shaded gates—extend towards and overlap with the location of the two dots (white dashed circles). The left and right plunger gates (LP and RP, respectively) are used to adjust the electrochemical potentials of the dots. Voltage pulses are also sent to these gates, through bias tees. White crossed boxes at the bottom indicate the location of Fermi reservoirs of electrons that are connected to the source and drain electrodes outside the image. **b**, Normalized transmission amplitude through the superconducting feedline, before the formation of dots. The applied microwave power is $P=-110$ dBm. From a Lorentzian fit (red solid line), the resonance frequency $f_0=5.7116$ GHz, loaded quality factor $Q\approx2{,}600$, internal quality factor $Q_i\approx5{,}780$ and coupling quality factor $Q_c\approx4{,}730$ are extracted[35]. **c**, Schematic cross-section of the device along the red dashed line in **a**. The double dot confining the electrons is formed in the strained Si quantum well layer by applying appropriate gate voltages to create a double-well potential. The resonator gates produce a tiny oscillating electric field E_r to which the electron in the DQD responds. Co micromagnets are located on top of the gate stack, isolated from the gates by a layer of SiN dielectric, and provide a transverse field gradient after they are magnetized by an external magnetic field B_{ext}. The gradient is not used intentionally in this experiment.

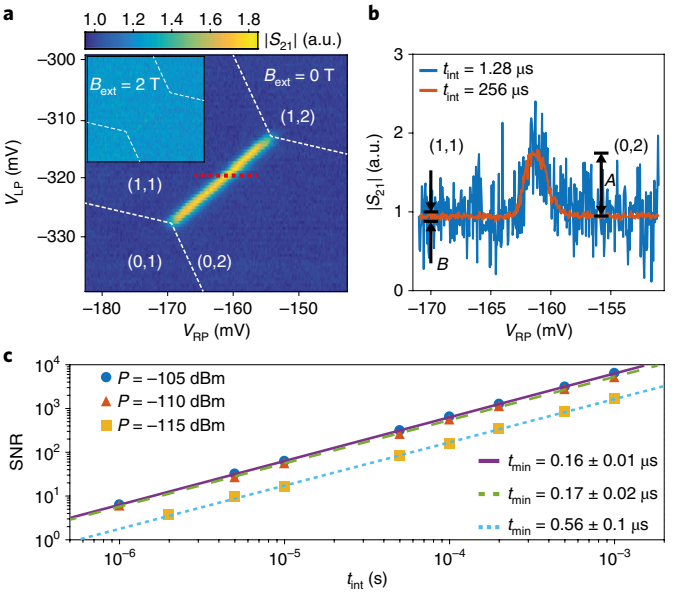

Fig. 2 | Characterization of the charge sensitivity. a,The transmitted amplitude at 5.7116 GHz and −110 dBm as a function of the voltages applied to LP and RP. The bright yellow line defines the zero detuning axis, along which one electron can tunnel freely between the left and right dots while a second electron remains in the right dot. White dashed lines indicate the boundaries of the charge stability diagrams, where electrons can be added to or removed from the dots. The tunnelling rates to the reservoirs were set well below f_0 (making these transitions undetectable by the resonator) to minimize effects from co-tunnelling[12]. The scan was taken by repeatedly applying a 500 Hz sawtooth wave to RP and stepping V_{LP} every 200 ms. Each pixel in the plot has an effective integration time of 1 ms. Inset: exactly the same scan in the presence of an external in-plane magnetic field of 2 T. Here, the probe frequency was set to 5.6930 GHz, to account for a shift of the resonance frequency with magnetic field. The overall transmission in the new frequency range is higher. White dashed lines in the inset are copied from the main plot. **b**, Transmitted amplitude versus the voltage on RP around zero detuning (red dashed line in **a**). Data are collected point by point in V_{RP}, with integration times of 1.28 μs (blue trace) and 256 μs (red trace). **c**, SNR as a function of integration time. Three sets of data are shown, corresponding to a power of −105 dBm (blue dots), −110 dBm (red triangles) and −115 dBm (yellow squares) through the feedline. Red data points were taken in a slightly different charge configuration from the blue and yellow data points. Each data set is fitted well by a straight line, from which we extrapolate t_{min}. The root-mean-square (r.m.s.) noise amplitude B was obtained from time traces containing 1,000 points for each integration time. Errors in A and B translate to uncertainties (standard deviation, s.d.) in SNR that are smaller than the size of the data points.

The data points follow $\mathrm{SNR}(t_{int})=t_{int}/t_{min}$, where t_{min} is the integration time for an SNR of unity. We find $t_{min}\approx170$ ns at −110 dBm input power, and it is ~3.3 times longer at −115 dBm, which is expected from the 5 dB difference in power. At higher power (−105 dBm), t_{min} begins to saturate, presumably because the electron displacement in the DQD reaches a maximum. The inverse resonator linewidth imposes a constraint on the minimum measurement time of $0.35(\kappa/2\pi)^{-1}\approx160$ ns. Using the following definition of the charge sensitivity, we obtain $\delta q=e\sqrt{t_{min}}=(4.1\pm0.3)\times10^{-4}\ e\ \mathrm{Hz}^{-1/2}$ at $P=-110$ dBm (with 1 s.d. uncertainty). This is an order of magnitude higher than reported for a microwave resonator probed with a quantum-limited Josephson parametric amplifier, but two orders of magnitude lower than the value reported without the parametric amplifier[29]. In the following experiment we set $P=-110$ dBm, where we have SNR ≈ 6 at 1 μs integration time, corresponding to a ~350 kHz bandwidth. The coupling strength between the DQD and resonator is ~175 MHz. We note that, in general, a larger coupling strength is beneficial for the charge sensitivity provided that the frequency shift is smaller than half the resonator linewidth. Beyond that, the signal saturates (for a fixed power).

Having characterized the charge sensitivity, we move on to detecting spin states. At $\varepsilon=0$, the S(1,1) and S(0,2) singlet states hybridize due to a finite interdot tunnel coupling t_c. Thus, when the system is in a singlet state, one electron is allowed to tunnel between the dots, loading the resonator as a result. When the system is in one of the triplet states, there is negligible hybridization of the (1,1) and (0,2) states at $\varepsilon=0$ (the valley splitting is estimated to be ~85 μeV from magnetospectroscopy; data not shown), so tunnelling is now prohibited and the resonator remains unaffected. At zero magnetic field the two electrons form a spin singlet ground state and a strong signal is observed at zero detuning, as discussed (Fig. 2a). When

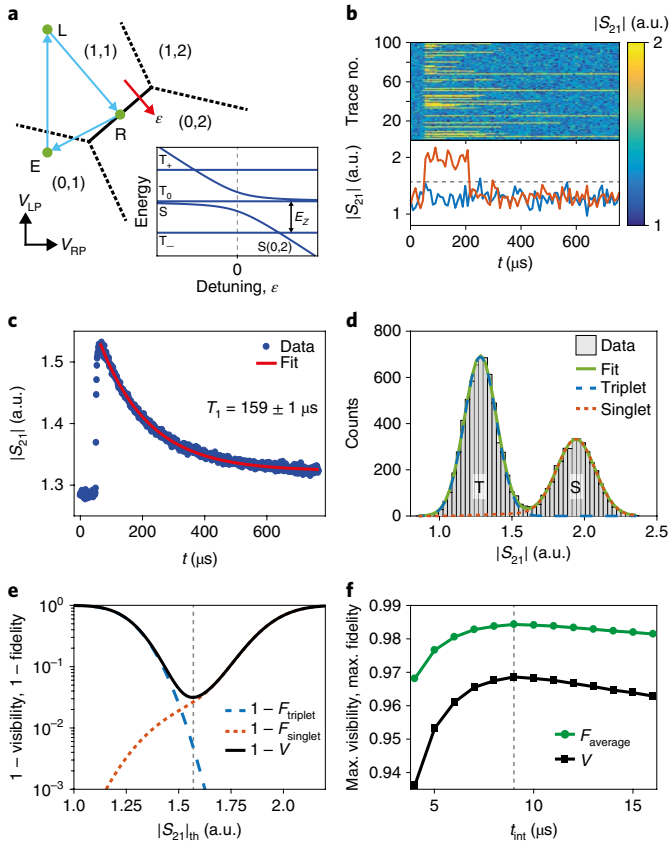

Fig. 3 | Single-shot spin read-out and fidelity analysis. a, Schematic of a typical charge stability diagram with a three-stage pulse sequence. The d.c. voltages on LP and RP are set to point R. A two-electron energy level diagram as a function of the detuning ε (red arrow) in a finite magnetic field is shown in the lower half. The $T_\pm$ states are separated from T_0 by $E_Z = g\mu_B B_{tot}$, where g is the g factor, μ_B is the Bohr magneton and B_{tot} consists of B_{ext} and the field from the micromagnets. Valley-orbit states are neglected in this diagram for simplicity. **b**, A total of 100 single-shot traces with 9 μs averaging time per data point are shown in the top panel as a function of time. The traces start 50 μs before pulsing to point R. The bright yellow lines correspond to the signal from the spin singlet state. Two traces are shown separately in the bottom panel. For the blue (red) line the electron was loaded into either T_0(1,1) or T_(1,1) (S(1,1)) at point L. The grey dashed line is the optimum threshold $|S_{21}|_{th} \approx 1.57$. **c**, Transmitted amplitude as a function of time shows a typical T_1 decay (blue dots). The error in T_1 corresponds to the s.d. of the exponential fit (red solid line). Data are taken at 2 T. **d**, Measured histogram of the single-shot traces with 9 μs integration time. A model adapted from ref. [32] was fitted to the data (green solid line) to extract the triplet (blue dashed line) and singlet (red dotted line) distributions. See main text for details. **e**, The calculated spin read-out fidelities and visibility as a function of threshold amplitude for 9 μs integration. The maximum visibility is found by setting the threshold at $|S_{21}|_{th} \approx 1.57$. **f**, Maximum average fidelity and visibility as a function of integration time. For each t_{int}, an analysis similar to that in **e** was performed.

we apply an external in-plane magnetic field B_{ext} of 2 T, the triplet state T_(1,1) becomes the ground state (Fig. 3a). As expected, this suppresses the signal from the S(1,1)–S(0,2) tunnelling significantly (inset, Fig. 2a). Here, we benefit from the resiliency of our resonator to high magnetic fields[21].

We probe the spin dynamics of our system by applying voltage pulses to gates LP and RP (Fig. 3a), first to empty the left quantum dot at point E (100 μs), then to load an electron with a random spin orientation into the left dot at point L (10 μs), and finally to measure the response of the resonator at point R. We perform 10,000 repetitions of this single-shot cycle, and record time traces of the transmitted signal with an integration time of 1 μs. The traces start 50 μs before pulsing to point R. The results from 100 cycles are shown in Fig. 3b (top panel) with an additional 9 μs integration time set in post-processing of the experimental data. We perform threshold detection, declaring a singlet (triplet) when the signal exceeds (does not exceed) a predefined threshold, $|S_{21}|_{th}$. Two examples of single traces are shown separately in the bottom panel. The blue trace reflects the case in which the two electrons form a spin triplet state; that is, the signal remains low during the entire trace. The red trace corresponds to loading a spin singlet state, which here decays to a T_(1,1) state after ~150 μs. When averaged over all traces, we obtain a characteristic decay with a relaxation time T_1 from the singlet to the triplet ground state of 159 μs (Fig. 3c). This value of T_1 is smaller than typical values for spins in silicon dots, possibly because it is measured at the charge degeneracy point and there is a strong transverse field gradient present along the interdot axis (see also ref. [30]). We expect that removing the transverse field gradient or orienting it perpendicular to the interdot axis would increase T_1. We note that the spin relaxation rate from the Purcell effect would be several orders of magnitude smaller[31]. Despite the short T_1, we can achieve high-fidelity single-shot read-out thanks to the high sensitivity and bandwidth of our resonator.

To characterize the spin read-out fidelity, we create a histogram of the signal integrated over the first 9 μs in point R. A clear bimodal distribution is visible in Fig. 3d. We fit the data to a model that is based on two noise-broadened Gaussian distributions with an additional term taking into account the relaxation of the singlet state during the measurement[32]:

$$N(|S_{21}|) = N_{tot}[P_S n_S + (1-P_S) n_T]|S_{21}|_{bin} \quad (1)$$

with

$$n_T = \frac{1}{\sqrt{2\pi}\sigma_T} e^{-\frac{(|S_{21}|-\mu_T)^2}{2\sigma_T^2}} \quad (2)$$

the triplet probability density and

$$n_S = \frac{1}{\sqrt{2\pi}\sigma_S} e^{-\frac{(|S_{21}|-\mu_S)^2}{2\sigma_S^2}} e^{-\frac{t_{int}}{T_1}} + \frac{1}{\sqrt{2\pi}\sigma_S}\frac{t_{int}}{T_1}\int_{\mu_T}^{\mu_S} \frac{1}{\mu_S-\mu_T} e^{-\frac{x-\mu_T}{\mu_S-\mu_T}\frac{t_{int}}{T_1}} e^{-\frac{(|S_{21}|-x)^2}{2\sigma_S^2}} dx \quad (3)$$

the singlet probability density. Here, μ_T (μ_S) is the average triplet (singlet) signal amplitude, σ_T (σ_S) is the s.d. of the triplet (singlet) peak, P_S is the probability of loading into S(1,1), and $|S_{21}|_{bin}$ is the bin size. We note that the singlet peak has a slightly larger spread than the triplet peak. This could be explained by the fact that in addition to the measurement noise that broadens the triplet signal, the singlet signal is also prone to the effects of charge noise.

We use the following definition of the read-out fidelities: $F_{triplet} = 1 - \int_{|S_{21}|_{th}}^{\infty} n_T d|S_{21}|$ and $F_{singlet} = 1 - \int_{-\infty}^{|S_{21}|_{th}} n_S d|S_{21}|$. The visibility is defined as $V = F_{triplet} + F_{singlet} - 1$. The maximum visibility for 9 μs averaging is 96.9% (Fig. 3e). The corresponding read-out fidelity for the singlet (triplet) is 97.3% (99.5%), with an average read-out fidelity of 98.4%. We repeat this analysis for various integration times (Fig. 3f). The average read-out fidelity is above 98% for t_{int} greater than 6 μs.

Extrapolating our results assuming a T_1 of 4.5 ms and $t_{int} = 16\,\mu s$, a spin read-out fidelity of 99.9% is possible, well above the fault-tolerance threshold. This integration time compares favourably to the millisecond coherence times of dynamically decoupled single spin qubits[33,34], even taking into account the duration of error correction pulses. Further improvements both in the duration and fidelity of spin read-out can be achieved by using quantum-limited amplifiers, such as a Josephson parametric amplifier or a travelling wave parametric amplifier. We expect an order of magnitude shorter read-out time to be feasible, assuming the amplifier noise remains the dominant noise source.

Although the read-out of singlet–triplet spin states is demonstrated here, this technique can also be applied to detecting addressable single spins provided that there is a reference spin. Manipulation of a single spin can be performed using a separate gate[30], so that the qubit frequency can be far detuned from the resonator frequency, minimizing the Purcell effect. Unwanted excitations due to a high probe frequency should be negligible provided that the frequency is far detuned from splittings such as the valley and Zeeman splittings.

The range of t_c that gives maximal resonator response (for a fixed power) depends on the DQD–resonator coupling strength. For the present tuning of the sample, a value of t_c below ~2 GHz would yield a resonator frequency shift of less than half the resonator linewidth, and would thus not achieve the maximum signal. The t_c can be tuned up to ~18 GHz while retaining full signal. However, for spin detection, the valley splitting in our device imposes in practice a much lower upper limit on t_c. An increased t_c leads to an increased intervalley tunnel coupling (between T_(1,1) and T_(0,2)), which can also be detected by the resonator when sufficiently large[11], giving the same signal as the singlet state for small valley splittings. A larger valley splitting should mitigate this effect.

In conclusion, we have used a high-Q and high-impedance on-chip superconducting resonator to demonstrate single-shot gate-based spin read-out in silicon within a few microseconds. Despite the relatively short T_1 in our system, we achieve a spin read-out fidelity up to 98.4% in less than 10 µs. The demonstration of single-shot gate-based spin read-out is a crucial step towards read-out in dense spin qubit arrays where it is not possible to integrate electrometers and accompanying reservoirs adjacent to the qubit dots. In contrast, multiple qubits on the inside of an array can be probed using a single resonator coupled to a word or bit line in a cross-bar architecture. Furthermore, a single feedline can be used for probing multiple resonators using frequency multiplexing. Moreover, this on-chip superconducting resonator is compatible with other implementations of silicon quantum dot qubits in a magnetic field.

Online content

Any methods, additional references, Nature Research reporting summaries, source data, statements of code and data availability and associated accession codes are available at https://doi.org/10.1038/s41565-019-0488-9.

Received: 31 December 2018; Accepted: 27 May 2019;
Published online: 8 July 2019

References

1. Zwanenburg, F. A. et al. Silicon quantum electronics. *Rev. Mod. Phys.* **85**, 961 (2013).
2. Vandersypen, L. M. K. et al. Interfacing spin qubits in quantum dots and donors—hot, dense and coherent. *npj Quantum Inf.* **3**, 34 (2017).
3. Ono, K., Austing, D. G., Tokura, Y. & Tarucha, S. Current rectification by Pauli exclusion in a weakly coupled double quantum dot system. *Science* **297**, 5585 (2002).
4. Elzerman, J. M. et al. Single-shot read-out of an individual electron spin in a quantum dot. *Nature* **430**, 431–435 (2004).
5. Hanson, R., Kouwenhoven, L. P., Petta, J. R., Tarucha, S. & Vandersypen, L. M. K. Spins in few-electron quantum dots. *Rev. Mod. Phys.* **79**, 1217 (2007).
6. Field, M. et al. Measurements of Coulomb blockade with a noninvasive voltage probe. *Phys. Rev. Lett.* **70**, 1311–1314 (1993).
7. Barthel, C. et al. Fast sensing of double-dot charge arrangement and spin state with a radio-frequency sensor quantum dot. *Phys. Rev. B* **81**, 161308 (2010).
8. Li, R. et al. A crossbar network for silicon quantum dot qubits. *Sci. Adv.* **4**, eaar3960 (2018).
9. Veldhorst, M., Eenink, H. G. J., Yang, C. H. & Dzurak, A. S. Silicon CMOS architecture for a spin-based quantum computer. *Nat. Commun.* **8**, 1766 (2017).
10. Colless, J. I. et al. Dispersive readout of a few-electron double quantum dot with fast rf gate sensors. *Phys. Rev. Lett.* **110**, 046805 (2013).
11. Betz, A. C. et al. Dispersively detected Pauli spin-blockade in a silicon nanowire field-effect transistor. *Nano Lett.* **15**, 4622–4627 (2015).
12. House, M. G. et al. Radio frequency measurements of tunnel couplings and singlet–triplet spin states in Si:P quantum dots. *Nat. Commun.* **6**, 8848 (2015).
13. Crippa, A. et al. Gate-reflectometry dispersive readout of a spin qubit in silicon. Preprint at https://arxiv.org/abs/1811.04414 (2018).
14. Pakkiam, P. et al. Single-shot single-gate rf spin readout in silicon. *Phys. Rev. X* **8**, 041032 (2018).
15. West, A. et al. Gate-based single-shot readout of spins in silicon. *Nat. Nanotechnol.* **14**, 437–441 (2019).
16. Urdampilleta, M. et al. Gate-based high fidelity spin read-out in a CMOS device. Preprint at https://arxiv.org/abs/1809.04584 (2018).
17. Gonzalez-Zalba, M. F., Barraud, S., Ferguson, A. J. & Betz, A. C. Probing the limits of gate-based charge sensing. *Nat. Commun.* **6**, 6084 (2015).
18. Rossi, A., Zhao, R., Dzurak, A. S. & Gonzalez-Zalba, M. F. Dispersive readout of a silicon quantum dot with an accumulation-mode gate sensor. *Appl. Phys. Lett.* **110**, 212101 (2017).
19. de Jong, D. et al. Rapid detection of coherent tunneling in an InAs nanowire quantum dot through dispersive gate sensing. *Phys. Rev. Appl.* **11**, 044061 (2019).
20. Samkharadze, N. et al. Strong spin–photon coupling in silicon. *Science* **359**, 1123–1127 (2018).
21. Samkharadze, N. et al. High-kinetic-inductance superconducting nanowire resonators for circuit QED in a magnetic field. *Phys. Rev. Appl.* **5**, 044004 (2016).
22. Cottet, A., Mora, C. & Kontos, T. Mesoscopic admittance of a double quantum dot. *Phys. Rev. B* **83**, 121311 (2011).
23. Petersson, K. D. et al. Circuit quantum electrodynamics with a spin qubit. *Nature* **490**, 380–383 (2012).
24. Frey, T. et al. Dipole coupling of a double quantum dot to a microwave resonator. *Phys. Rev. Lett.* **108**, 046807 (2012).
25. Chorley, S. J. et al. Measuring the complex admittance of a carbon nanotube double quantum dot. *Phys. Rev. Lett.* **108**, 036802 (2012).
26. Landig, A. J. et al. Microwave cavity detected spin blockade in a few electron double quantum dot. Preprint at https://arxiv.org/abs/1811.03907 (2018).
27. Schuster, D. I. et al. AC Stark shift and dephasing of a superconducting qubit strongly coupled to a cavity field. *Phys. Rev. Lett.* **94**, 123602 (2005).
28. Mizuta, R., Otxoa, R. M., Betz, A. C. & Gonzalez-Zalba, M. F. Quantum and tunneling capacitance in charge and spin qubits. *Phys. Rev. B* **95**, 045414 (2017).
29. Stehlik, J. et al. Fast charge sensing of a cavity-coupled double quantum dot using a Josephson parametric amplifier. *Phys. Rev. Appl.* **4**, 014018 (2015).
30. Mi, X. et al. A coherent spin–photon interface in silicon. *Nature* **555**, 599–603 (2018).
31. Bienfait, A. et al. Controlling spin relaxation with a cavity. *Nature* **531**, 74–77 (2016).
32. Barthel, C., Reilly, D. J., Marcus, C. M., Hanson, M. P. & Gossard, A. C. Rapid single-shot measurement of a singlet–triplet qubit. *Phys. Rev. Lett.* **103**, 160503 (2009).
33. Veldhorst, M. et al. An addressable quantum dot qubit with fault-tolerant control-fidelity. *Nat. Nanotechnol.* **9**, 981–985 (2014).
34. Yoneda, J. et al. A quantum-dot spin qubit with coherence limited by charge noise and fidelity higher than 99.9%. *Nat. Nanotechnol.* **13**, 102–106 (2018).
35. Khalil, M. S., Stoutimore, M. J. A., Wellstood, F. C. & Osborn, K. D. An analysis method for asymmetric resonator transmission applied to superconducting devices. *J. Appl. Phys.* **111**, 054510 (2012).

Acknowledgements

The authors thank T.F. Watson, J.P. Dehollain, P. Harvey-Collard, U.C. Mendes, B. Hensen and other members of the spin qubit team at QuTech for useful discussions, L.P. Kouwenhoven and his team for access to NbTiN films, and P. Eendebak and L. Blom for software support. This research was undertaken thanks in part to funding from the European Research Council (ERC Synergy Quantum Computer Lab), the

Netherlands Organisation for Scientific Research (NWO/OCW) as part of the Frontiers of Nanoscience (NanoFront) programme and Intel Corporation.

Author contributions

G.Z., N.S. and L.M.K.V. conceived and planned the experiments. G.Z. and M.L.N. carried out the experiments. A.S. grew the heterostructure with G.S.'s supervision. N.S. designed and fabricated the device. D.B. and N.K. contributed to sample fabrication. G.Z., M.L.N. and L.M.K.V. analysed the results. G.Z. and L.M.K.V. wrote the manuscript with input from all co-authors. L.M.K.V. supervised the project.

Competing interests

The authors declare no competing interests.

Additional information

Supplementary information is available for this paper at https://doi.org/10.1038/s41565-019-0488-9.

Reprints and permissions information is available at www.nature.com/reprints.

Correspondence and requests for materials should be addressed to L.M.K.V.

Peer review information: *Nature Nanotechnology* thanks Hongwen Jiang and the other, anonymous, reviewer(s) for their contribution to the peer review of this work.

Methods

The Si/SiGe heterostructure was grown on an n-type Si(100) substrate in a reduced-pressure vapour deposition reactor. The layer sequence consisted of (from bottom to top) a $Si_{0.7}Ge_{0.3}$ virtual substrate, a 10-nm-thick strained Si quantum well, a 30-nm-thick $Si_{0.7}Ge_{0.3}$ barrier and a 1-nm-thin Si cap. A layer of 20-nm-thick Al_2O_3 was deposited in the DQD region by atomic-layer deposition. The 25-nm-thick Al gates on the gate oxide were fabricated using electron-beam lithography, evaporation and a liftoff process. The Ti/Co (5 nm/200 nm thick) micromagnets were insulated from the gates with 30-nm-thick sputtered SiN. The on-chip superconducting resonator (~100 nm width), feedline and ground planes were defined using reactive ion etching (SF_6/He) of a 14-nm-thick sputtered NbTiN layer.

The device was cooled to ~11 mK in a dilution refrigerator. The microwave response was measured using standard heterodyne detection. One of the two microwave sources was used to send a signal with frequency 5.7116 GHz (5.6930 GHz at 2 T) to the feedline, through heavily attenuated semi-rigid coaxial cables. The transmitted response was first amplified at ~4 K using a commercial cryogenic amplifier, then amplified a second time at room temperature using another commercial amplifier. The signal was demodulated using an IQ mixer, with a reference signal (5 MHz offset) from the second microwave source. The in-phase and quadrature components were filtered and amplified before being recorded by a giga-sample waveform digitizer to extract the transmitted signal amplitude and phase. The 500 Hz sawtooth wave used for producing the stability diagram as well as the voltage pulses used for unloading and loading an electron were generated by an arbitrary waveform generator. See Supplementary Fig. 2 for details of the electronic instruments and microwave components.

Data availability

The data reported in this paper are archived at https://doi.org/10.4121/uuid:8df1a6fa-9230-400f-a790-1b7714b1aad5.